scientific reports



OPEN

A comparative analysis of mercury intrusion and nitrogen adsorption methods for multifractal characterization of shale reservoirs in northern Songliao Basin

Siyu Chen¹, Dameng Liu¹⊠, Yingjin Wang², Weifeng Zhang³, Qingwei Zheng³ & Xinran Yin⁴

The northern Songliao Basin is shale-oil-rich with high exploration potential. However, its heterogeneity challenge reservoir characterization and evaluation, impeding exploration and development efforts. Thus, analyzing continental shale's pore structure and heterogeneity is crucial. This work utilizes High-pressure mercury intrusion (HMIP) and low-pressure N_2 adsorption (LPN_2A) methods to analyze the multifractal characteristics of shale pore structures at different depths. Results indicate that there is no significant correlation between the pore structures determined by the two methods. However, the heterogeneity of the pore structure obtained by the HMIP method is stronger than that by the LPN_2A method. The study also found that as the total pore volume increases, the heterogeneity of the pore structure increases, while the pore connectivity is not significantly correlated with the pore volume. In addition, mineral content has a significant impact on the heterogeneity of pore structure and pore size distribution, especially the content of quartz.

 $\textbf{Keywords} \quad \text{Multifractal characterization, High-pressure mercury intrusion, Low-pressure N}_2 \text{ adsorption, Oil shale}$

After years of exploitation, easily accessible conventional oil and gas reservoirs are depleting, with output waning and costs rising. To satisfy escalating energy demands, new areas are being explored beyond traditional source^{1–3}. Unconventional oil and gas have become a global focus, especially post the U.S. shale breakthrough, with production escalating annually⁴. By 2020, U.S. shale oil output accounted for 60%, outpacing Saudi Arabia to top the world⁵. Unconventional reservoirs, deeper and more complex than conventional ones, are garnering more interest^{6–14}. The terrestrial shale oil in the Songliao Basin of China has enormous development potential. Shale is a heterogeneous multi-layered porous medium, exhibiting high interlayer and intralayer heterogeneity on a macroscopic level, and on a microscopic level, it exhibits the heterogeneity of the complex pore-fracture system of shale. The heterogeneity of shale pore structure will affect the macroscopic heterogeneity of the reservoir to a certain extent, and thus affect the permeability, seepage, and production performance of shale oil and gas in all directions.

Generally, the characteristics of the pore structure are obtained by injecting different fluids into the core. The mercury injection method is commonly used to characterize the pore structure features of shale reservoirs^{15–17}, first proposed by H.L. Ritter and L.C. Drake. It is used to measure the capillary pressure curve of the sample; the greater the external pressure, the smaller the pore radius that mercury can enter, thereby obtaining the pore size distribution information^{17–20}. Due to the ultra-low porosity and ultra-low permeability of shale's rock physical properties, liquid mercury theoretically cannot enter excessively small pores (<50 nm). Nitrogen adsorption/desorption is a common method for characterizing nanoscale pores, often used for the characterization of micropores and mesopores in porous materials, with a test range of 1.7–300 nm. Based on the shape of the isotherm curve, one can infer the size and distribution of the material's pores. By analyzing the data from the

¹School of Energy Resources, China University of Geosciences, Beijing 100083, China. ²School of Resources and Environmental Engineering, Hefei University of Technology, Hefei 230009, China. ³China National Logging Corporation, Daqing Branch, Daqing 163000, China. ⁴Lusheng Petroleum Development Co., Ltd., Shengli Oilfield Company, SINOPEC, Dongying 257000, Shandong, China. [△]email: dmliu@cugb.edu.cn

two tests mentioned above, the heterogeneity of the core can be judged. To quantitatively characterize the heterogeneity and apply it to other strata, fractal theory is introduced^{21,22}.

Fractal theory is a simple yet powerful tool for studying objects with self-similarity²³. In recent years, fractal theory and models have been widely applied to the study of reservoir physical property characteristics^{7,24}. Examples include the fractal BET model (Brunauer–Emmett–Teller Model) method, the fractal FHH (Frenkel–Halsey–Hill) model method, and thermodynamic model methods^{25–30}. However, a single fractal dimension works well in reservoirs with simple pore structures but cannot accurately reflect the physical property characteristics of complex reservoirs³¹. Scholars, in order to quantitatively characterize the heterogeneity of porous media^{2,32–35}, have introduced multifractal theory. Multifractal parameters (such as multifractal dimension D_q , singularity index $\Delta \alpha$) are closely related to the pore structure and pore size distribution characteristics of the reservoir^{31,36}. Multifractals divide complex structures into different regions, which are collections composed of single fractals, so they can provide more comprehensive information for the study of reservoir physical property characteristics.

The continental shale oil in Songliao Basin is a promising unconventional reserve in China. Understanding pore structure characteristics at different burial depths is crucial for its exploration and development. Given that shales with similar burial depths may share analogous depositional environments, which could result in calculated multifractal dimensions that do not vary significantly. We have selected shale samples from different depths for experimentation and analysis to investigate the factors influencing the multifractal dimensions of shales. This study collected eight shale oil samples from various burial depths in the Y1 well, Songliao Basin, China. Using HMIP and LPN₂A methods, we aimed to: (1) analyze pore size distribution, (2) derive multifractal characteristics, and (3) explore the relationship between multifractal parameters and sample physical properties.

Geological setting

The Songliao Basin is located in the northeastern part of China, within the provinces of Heilongjiang, Jilin, and Liaoning (Fig. 1a), surrounded by hills and mountains, with a northeast-trending long axis, 750 km long, 330-370 km wide, and an area of 26×10^4 km^{2,37-39} (Fig. 1b), and is one of the most oil and gas resourcerich continental sedimentary basins discovered in the world. The fault-basin complex, primarily composed of the Mesozoic and Cenozoic strata, is formed on the Hercynian folded basement and exhibits a double-layer structure with a lower fault and an upper depression, with the upper part being the unified depression layer of the basin and the lower part being a group of separated fault basins 40-42. Controlled by the basement faults, the fault basins within the basin are distributed in a north-northeast direction, with larger fault basins in the central and eastern parts, developing in a continuous belt. It was the largest Cretaceous tectonic freshwater to slightly saline lake basin on the Asian ancient land, and during its development, it experienced multiple expansions and contractions accompanying crustal uplift and subsidence movements^{34,43,44}. The main strata developed during this period include the Lower Cretaceous (including the Huoshiling Formation, Shahezi Formation, Yingcheng Formation, Denglouku Formation, and Quantou Formation), Upper Cretaceous (Qingshankou Formation, Yaojia Formation, Nenjiang Formation, Sifangtai Formation, and Mingshui Formation), and Cenozoic strata. The basin has experienced two large-scale water invasions; the first occurred during the deposition of the Upper Cretaceous Qingshankou Formation, with a widespread deep lake to half-deep lake environment, depositing a thick dark shale of about 320 m, mainly in the Qijia-Gulong depression and the Daqing placanticline (Fig. 1c). The second was during the deposition of the first and second members of the Cretaceous Nenjiang Formation, when the lake water covered the entire Songliao Basin, marking the largest water invasion in the basin's sedimentary history, with a thickness of dark shale reaching 300 m^{38,40,45,46}. During the depositional periods of the Qingshankou Formation and Nenjiang Formation, the lake basin had a large distribution area, deep water body, and a rich variety of organisms, with abundant organic matter sources and favorable preservation

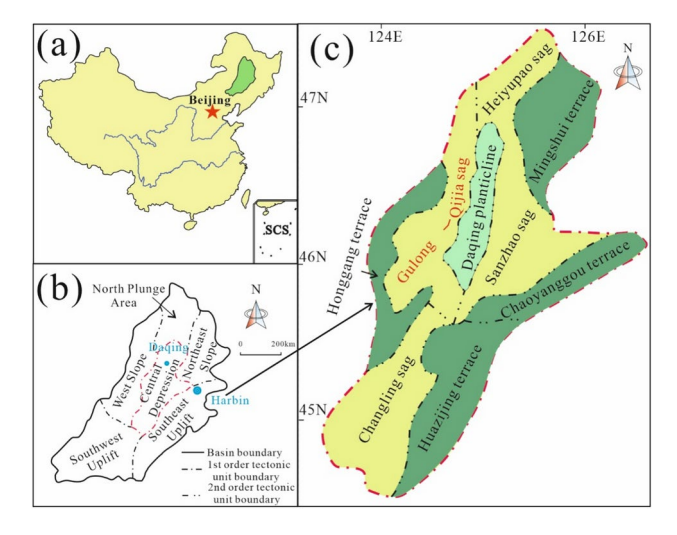


Fig. 1. (a) Location map of Songliao Basin; (b) 1st order tectonic unit in Songliao Basin; (c) 2nd order tectonic unit in Songliao Basin. Modified by Li et al. ⁴⁷.

conditions, laying the material foundation for the large-scale enrichment of continental shale oil in the shallow layers of the northern Songliao Basin.

Methodology

The experimental samples in this paper are laminated black shales from different depth intervals, all collected from the Y1 well located in the northern part of the Songliao Basin, specifically selecting eight shale core samples from a depth range of 2340 m to 2440 m.

Petrographic composition tests

In this study, the microstructure and composition of the samples were observed using Scanning Electron Microscope (SEM). Quantitative characterization of rock composition were carried out in accordance with the standards GB/T 19145-2022 "Determination for total organic carbon in sedimentary rock standard procedure" and SY/T 5163-2018 "Analysis method for clay minerals and ordinary non-clay minerals in sedimentary rocks" by the X-ray diffraction standard procedure.

Nitrogen adsorption/desorption

Low-temperature N₂ adsorption/desorption: In accordance with GB/T 19587-2017 "Determination of the specific surface area of solids" by gas adsorption using the *BET* method, 10 g of sample with a mesh size of 60–80 is first degassed and dried for 24 h, followed by low-temperature N₂ adsorption/desorption experiments at a condition of 77K. The *BET* and *BJH* models are employed to obtain the specific surface area and pore size distribution of N₂ adsorption, respectively.

Mercury intrusion porosimetry

High-pressure mercury intrusion experiment: Referring to GB/T 29171-2023 "Rock capillary pressure measurement standard", before conducting the test, samples must be prepared into 1 cm³ cubes, and the samples also need to be continuously dried at 105 °C for 8 h to ensure that the original pores of the coal samples are not destroyed by high temperatures and to effectively remove impurities and gases within them. During the testing process, it is essential to ensure that the surface of the samples is smooth to avoid the "Hemp effect". The mercury intrusion test measures the pore size with a lower limit of 3 nm and an upper limit reaching several hundred micrometers.

Multifractal analysis

Many scholars, after analyzing the mercury intrusion and liquid nitrogen data of samples, believe that rocks possess multifractal characteristics, and that multifractal parameters are closely related to the pore system of the core samples 48,49 . This paper employs the box-counting method to perform multifractal analysis on the test data of rock samples saturated with water. In the analysis process, the object of study is divided into N boxes equally, with the size of each box being ε . The probability mass distribution function of the ε -sized I-th box can be represented as:

$$P_i(\varepsilon) = \frac{N_i(\varepsilon)}{\sum_{i=1}^{N(\varepsilon)} N_i(\varepsilon)}$$
 (1)

where $N_i(\varepsilon)$ is the cumulative porosity or cumulative pore volume of interval *i*. $P_i(\varepsilon)$ is the probability mass function.

If the samples have multifractal characteristics, the probability mass function $P_i(\varepsilon)$ and the box size ε have an exponential relationship, which can be expressed as⁵⁰:

$$P_i\left(\varepsilon\right) \propto \varepsilon^{\alpha_i}$$
 (2)

where α_i is the Lipschitz-Hölder singularity exponent, and the position of the box affects the value of α_i . $N_{\alpha}(\varepsilon)$ is the number of boxes with the same α value, and $N_{\alpha}(\varepsilon)$ conforms to⁵⁰:

$$N_{\alpha}\left(\varepsilon\right) \propto \varepsilon^{-f\left(\alpha\right)}$$
 (3)

where $f(\alpha)$ is the spectrum of the fractal dimensions formed by boxes with the same α value, and the relationship between $f(\alpha)$ and α is a unimodal curve. Both $\alpha(q)$ and $f(\alpha)$ can be calculated based on the following equations:

$$\alpha\left(q\right) \propto \frac{\sum_{i=1}^{N(\varepsilon)} \left(u_i(q,\varepsilon) \times \ln p_i(\varepsilon)\right)}{\ln(\varepsilon)} \tag{4}$$

$$f(q) \propto \frac{\sum_{i=1}^{N(\varepsilon)} \left(u_i(q,\varepsilon) \times \ln u_i(\varepsilon)\right)}{\ln(\varepsilon)} \tag{5}$$

where

$$u_i\left(q,\varepsilon\right) = \frac{P_i^q(\varepsilon)}{\sum_{i=1}^{N(\varepsilon)} P_i^q(\varepsilon)} \tag{6}$$

where q is an order of the matrix, and the value range is from $-\infty$ to $+\infty$. The value of q is an integer in the interval [-10,10]. The denominator in Eq. (6) is the partition function. It can be expressed as⁴⁷:

$$X(q,\varepsilon) = \sum_{i=1}^{N_i} P_i^q(\varepsilon) \propto \varepsilon^{-(q-1)D_q}$$
(7)

where D_q is the generalized dimension related to q, which can be defined as⁵¹:

$$D_{q} = \frac{1}{q-1} \lim_{\varepsilon \to 0} \frac{\log \sum_{i=1}^{N(\varepsilon)} p_{i}^{q}(\varepsilon)}{\log \varepsilon}$$
 (8)

As for q, when q < 0, D_q represents the low probability measurement region for aperture; On the contrary, D_q represents the low probability measurement region for aperture⁵². Meanwhile, the mass exponent $\tau(q)$ of a q-order matrix can be defined as:

$$\tau\left(q\right) = -\lim_{\varepsilon \to 0} \frac{\log X(q,\varepsilon)}{\log \varepsilon} = -\lim_{\varepsilon \to 0} \frac{\sum_{i=1}^{N(\varepsilon)} P_i^q(\varepsilon)}{\log \varepsilon} \tag{9}$$

Combining Eqs. (8) and (9), the mass exponent $\tau(q)$ can be expressed as 50 :

$$\tau\left(q\right) = \left(1 - q\right)D_{q}\tag{10}$$

Through the Legendre transformation⁵¹, relationships between the singularity strength $\alpha(q)$ and q and $\tau(q)$ can be expressed as⁵¹:

$$\alpha\left(q\right) = \frac{d\tau(q)}{dq} \tag{11}$$

$$f(\alpha) = q\alpha(q) - \tau(q) \tag{12}$$

Generally, the multifractal dimension D_q and singularity strength range $\Delta\alpha$ ($\Delta\alpha=\alpha_{max}-\alpha_{min}$) are two important parameters used to study the multifractal characteristics, singularity, and heterogeneity of the pore structures of porous media⁵³. In multifractal analysis, the fractal dimension D_q is a spectrum that changes with scale, offering a detailed measure of fractal complexity. The singularity strength range $\Delta\alpha$ is the spread of the singularity strength exponent α across multifractal analysis. α indicates the singularity level in different parts of the fractal. A larger $\Delta\alpha$ signifies a strong multifractal, while a smaller $\Delta\alpha$ suggests a weak one, approaching a mono-fractal^{51,53}.

Results

Petrographic description

Scanning electron microscopy observations reveal that the main mineral components of the continental shale in this study include quartz, feldspar, and clay minerals, with trace amounts of pyrite also observable. The micro storage spaces of the shale mainly consist of fractures and pores, which are further divided into intergranular pores, intragranular pores, and organic matter pores, among others. The shapes of the pores include spherical, flocculent, strip-like, and amorphous forms. Quartz particles are enriched in three forms: laminar strip-like, amorphous lump-like, or sporadic distribution within the shale minerals. Clay minerals are predominantly lamellar. Fractures are highly developed; under scanning electron microscopy, intercrystalline fractures, intracrystalline fractures, and a few dissolution seams can be observed. Under optical microscopy, common fractures include interlayer fractures and quartz-filled fractures, with quartz-filled fractures generally parallel to the stratification, occasional organic matter bands, and it is rare to see reticular fractures or fractures perpendicular to the stratification (Fig. 2).

In accordance with the standards GB/T 19145-2022 "Determination for total organic carbon in sedimentary rock standard procedure" and SY/T 5163-2018 "Analysis method for clay minerals and ordinary non-clay minerals in sedimentary rocks" by the *X-ray* diffraction standard procedure, foundational experimental tests were conducted on the samples. The basic information of the samples can be found in Table 1:

LPN₂A pore structure characterization

Figure 3 displays the LPN₂A adsorption and desorption isotherms of the shale samples. A distinct hysteresis loop is formed between the adsorption curve and the desorption curve of the samples. According to the IUPAC classification, the adsorption/desorption curves of the samples are of type "H2" (The mesh effect, generated by the complex pore structure, plays an important role here). The desorption line shows a sharp decline at a relative pressure of 0.4 to 0.5, indicating that the samples corresponding to such curves have well-developed ink-bottle-shaped pores with wide bodies and narrow throats.

Table 2 shows the results of the LPN_2A analysis for pore volume and specific surface area. The total pore volume and specific surface area of the samples range from 0.033 to 0.043 cm³/g and 22.473 to 36.383 m²/g, respectively. The average pore diameter is between 4.748 and 5.869 nm. According to International Union of Pure and Applied Chemistry (IUPAC) classification, it can be seen that the sample mainly develops mesopores (pore size from 2 to 50 nm as per IUPAC classification) and macropores (pores bigger than 50 nm) develop slightly larger than micropores (pores smaller than 2 nm)²1,2².

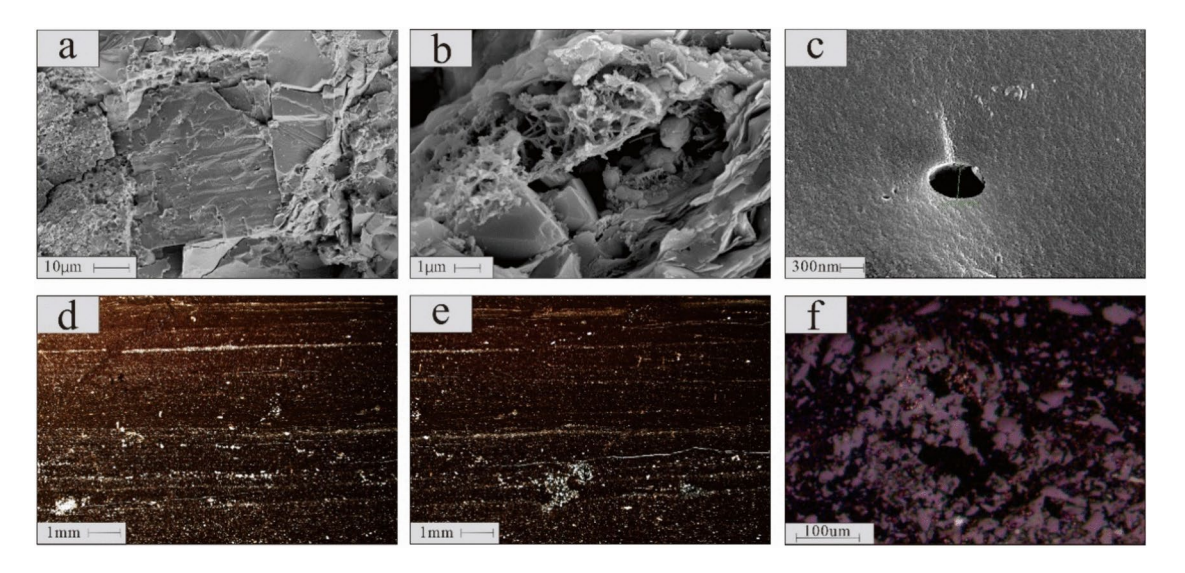


Fig. 2. Microscopic characteristics of scanning electron microscope and thin section of reservoir rocks. (a) Intragranular and intergranular pores; (b) Intergranular pores in illite; (c) Spherical organic matter pore; (d) Bedding and microfractures; (e) Quartz particle clumps; (f) Organic matter accompanied by pyrite development pores.

			Mineral content (%)								
								Clay Minerals			
Sample no.	Depth (m)	TOC (%)	Quartz	Feld-spar	Calcite	Dolomite	Pyrite	Total	(I	С	I/S)
Y1-1	2341	2.84	35.3	22.5	0.0	2.9	4.3	35.0	(58	15	27)
Y1-2	2345	2.09	35.6	29.5	1.1	0.0	4.1	29.6	(72	7	21)
Y1-3	2349	1.99	35.5	16.7	1.3	0.0	6.3	40.2	(69	7	24)
Y1-4	2354	1.78	35.2	30.4	1.5	0.0	3.5	29.3	(63	16	21)
Y1-5	2358	1.70	36.7	28.8	0.0	0.0	3.9	30.6	(68	10	22)
Y1-6	2366	1.89	35.0	27.3	0.9	0.0	4.0	32.9	(71	8	21)
Y1-7	2391	2.11	34.5	20.5	0.8	0.0	3.9	39.4	(59	9	32)
Y1-8	2432	3.27	36.7	10.3	4.4	0.0	0.0	48.6	(63	5	32)

Table 1. Sample information and basic parameters. *TOC* Total organic carbon; *I* Illite; *C* Chlorite; *I/S* Illitesmectite mixed layer; *Total* Illite+chlorite+illite-smectite.

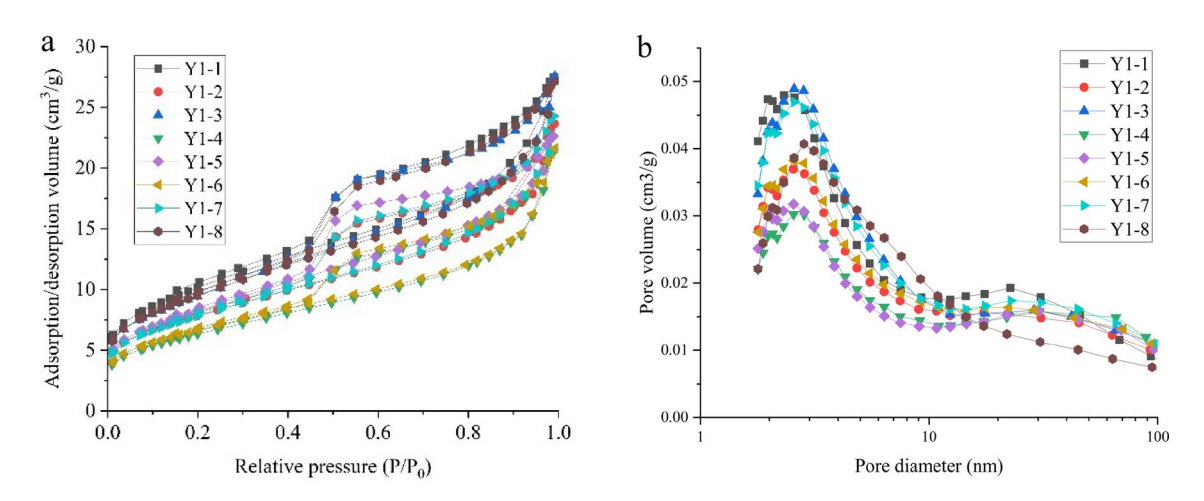


Fig. 3. (a) Low-temperature nitrogen adsorption and desorption isotherms of all samples; (b) Distributions of incremental pore volumes and specific surface areas of shale samples.

			Percentage content of pores in different pore sizes (%)		
Sample no.	Pore volume (cm ³ /g)	Surface area (m ² /g)	<2 nm	2-50 nm	>50 nm
Y1-1	0.042	36.383	17.34	79.07	3.59
Y1-2	0.037	27.739	15.18	79.92	4.90
Y1-3	0.043	33.825	14.94	80.80	4.26
Y1-4	0.033	22.473	13.76	79.54	6.70
Y1-5	0.033	23.559	15.39	78.90	5.71
Y1-6	0.038	27.793	5.33	80.20	14.47
Y1-7	0.043	33.576	4.59	80.19	15.23
Y1-8	0.036	27.628	3.42	84.58	12.01

Table 2. Characteristics of pore structure by LPN_2A .

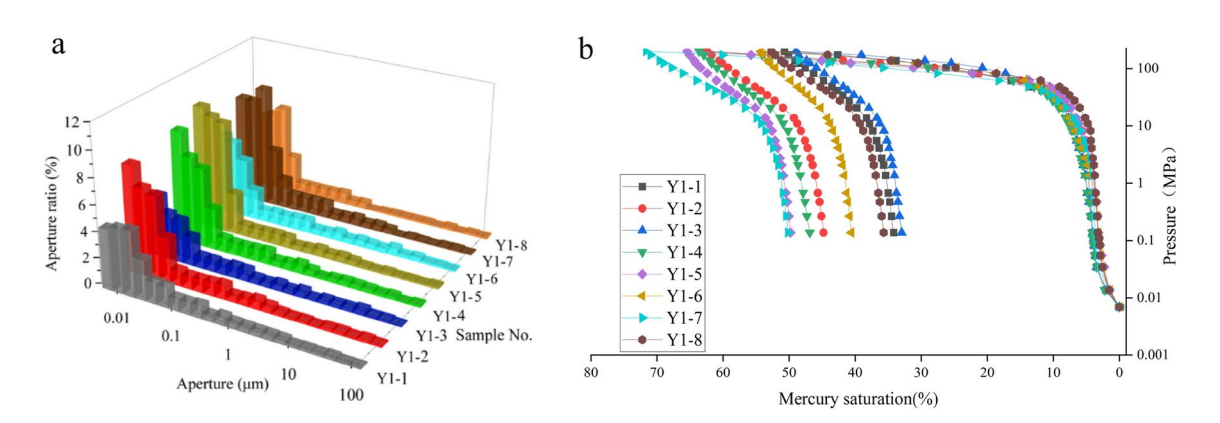


Fig. 4. (a) Histogram of mercury intrusion pore characteristics for all samples; (b) Intrusion/withdrawal mercury curve of shale samples.

HMIP pore structure characterization

Based on the differences in the openness and connectivity of the shale reservoir pores, the pores are classified into closed pores, semi-closed pores, and open pores, with the latter two constituting the effective storage space of the reservoir. The "hysteresis loop" feature of the mercury intrusion curve can be used to analyze the openness and connectivity of the pores. Samples with developed open pores can form a hysteresis loop with the advancing and receding mercury curves. Samples with developed semi-closed pores usually do not have a distinct hysteresis loop. However, the bottleneck pores, as a special type of semi-closed pores, have a difference in the receding mercury pressure corresponding to the bottleneck and the body, thus forming a drop-type hysteresis loop, but their pore connectivity is poor. The advancing/retracting mercury curves and the hysteresis loop characteristics formed in the study area are similar, indicating that the pore structure characteristics of the shale in the study area are similar. Figure 4 shows the HMIP measurement results and the pore size distribution characteristics of the samples in the study area. The advancing mercury curve of the samples steadily rises as the pressure increases at low pressures, then the increase in mercury intrusion slows down, and at the high-pressure stage, the cumulative mercury intrusion shows a rapid increase again, indicating the presence of large-diameter macropores and small-diameter micropores in such shales, while pores of intermediate diameter are relatively underdeveloped, showing a bimodal pore size distribution characteristic. The retracting mercury curve shows gradual mercury retraction at the beginning and tends to be flat later, indicating that the large-diameter pores have good openness and connectivity at the stage, and due to the lack of communication with intermediate-scale pores, the connectivity of the micropores is poor, making the later stage of mercury retraction not obvious. The advancing and retracting mercury curves have a narrow hysteresis loop, with a small difference between the advancing and retracting mercury volumes, indicating that such samples have a large proportion of semi-closed pores, the pore openness is not ideal, which is not conducive to the permeation and migration of fluids, and the storage conditions are also poor.

Table 3 shows that the total pore volume of the samples is 0.63 to 1.02 cm 3 /g. And the pore size distribution characteristics indicate that the shale in the study area is mainly dominated by mesopores of 2-50 nm (76.84% to 88.32%), with macropores being the least (11.68% to 23.16%), followed by non-micropores smaller than 2 nm.

Multifractal characteristics

Figure 5 shows the relationship between the mass distribution function $\tau(q)$ and the variable q for the 8 samples (with a step size of 1 for q). The mass distribution function reflects the fractal characteristics of the pore size distribution⁴⁹. If the mass distribution function $\tau(q)$ has a linear relationship with the variable q, it indicates that

			Percentage content of pores in different pore sizes (%)		
Sample no.	Pore volume (cm ³ /g)	Surface area (m ² /g)	<2 nm	2-50 nm	>50 nm
Y1-1	0.77	27.56	0	76.84	23.16
Y1-2	0.63	21.10	0	83.16	16.84
Y1-3	0.80	26.59	0	77.62	22.38
Y1-4	0.68	21.56	0	81.32	18.68
Y1-5	0.70	21.60	0	85.15	14.85
Y1-6	0.85	28.68	0	79.36	20.64
Y1-7	0.85	29.28	0	80.14	19.86
Y1-8	1.02	23.56	0	88.32	11.68

Table 3. Characteristics of pore structure by *HMIP*.

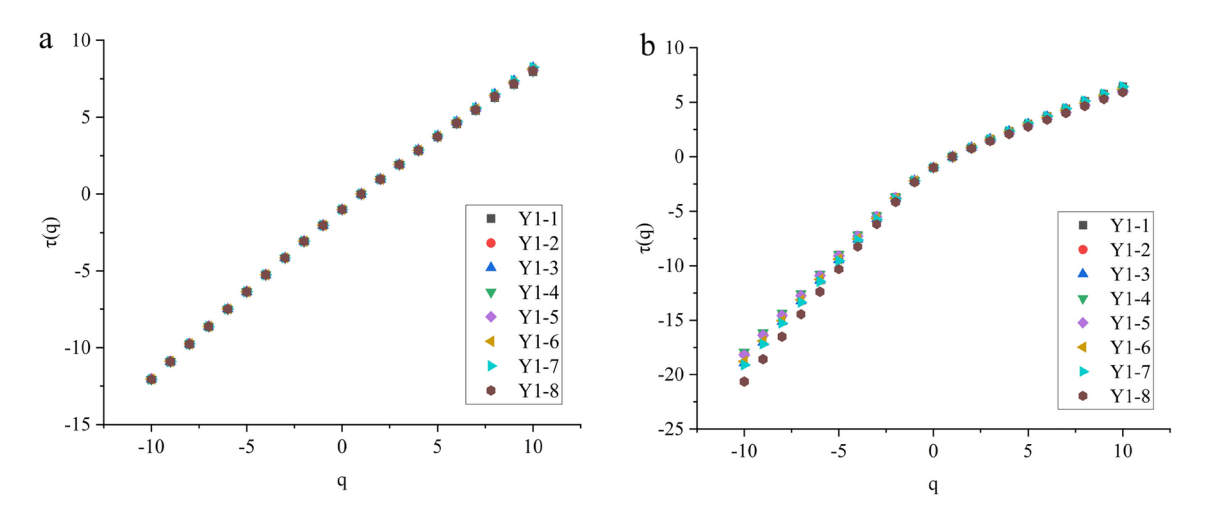


Fig. 5. The relationship between the $\tau(q)$ and q: (a) LPN_2A , (b) HMIP.

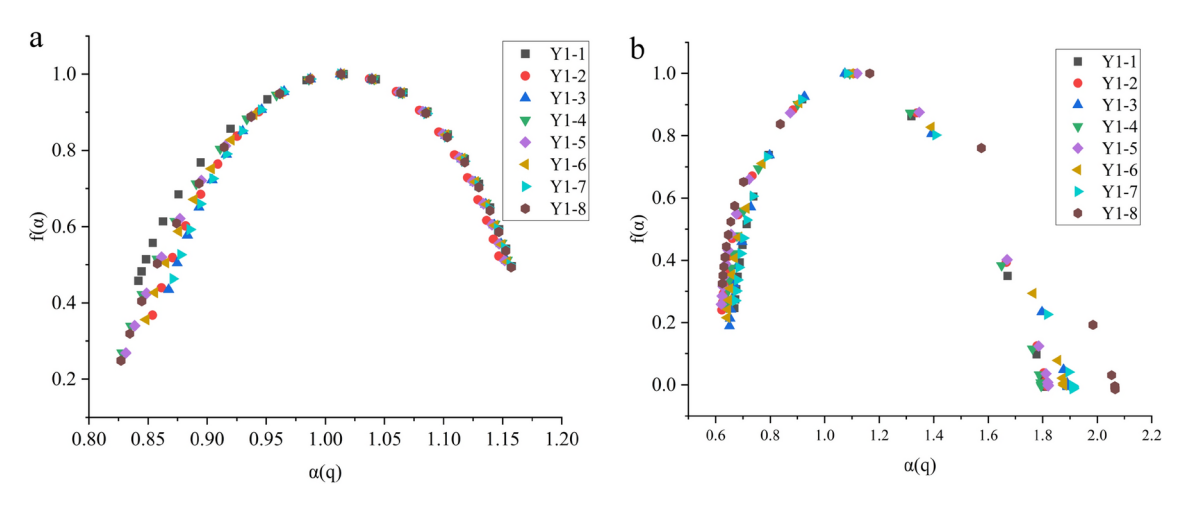


Fig. 6. The relationship between the f(a) and a(q): (a) LPN_2A , (b) HMIP.

the pore system of the sample is homogeneous and the sample does not have fractal characteristics. As shown in the figure, as the variable q increases, the mass distribution function $\tau(q)$ also increases. According to its trend, the graph can be divided into two segments. In the low-probability measurement area (q < 0), as q increases, the mass distribution function $\tau(q)$ increases significantly. In the high-probability measurement area (q > 0), the mass distribution function $\tau(q)$ also increases with the increase of q, but the trend tends to be flat.

Figure 6 is the multifractal spectrum graph for the 8 samples. The shape and symmetry of the multifractal spectrum graph can reflect the singularity information of the samples⁵⁴. As shown in the figure, the multifractal

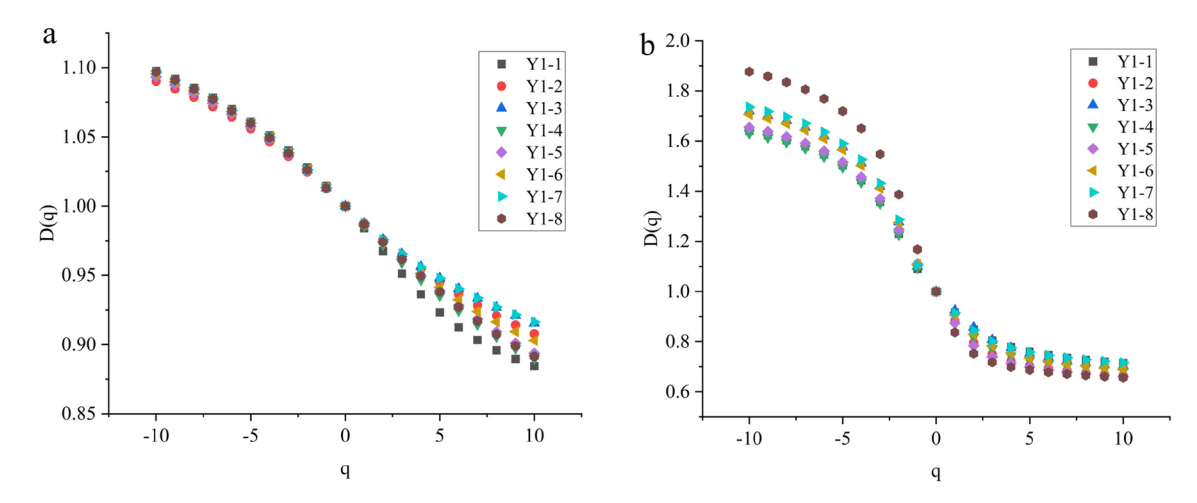


Fig. 7. Generalized dimension (D_q) versus variable q from q = -10 to q = 10: (a) LPN_2A , (b) HMIP.

	HMIP/LPN ₂ A						
Sample no.	D(0)	D(1)	D(2)	D(0)-D(1)	D(-10)	D(10)	
Y1-1	0.99/0.99	0.92/0.98	0.85/0.97	0.08/0.02	1.64//1.10	0.72//0.21	
Y1-2	0.99/0.99	0.88/0.99	0.80/0.98	0.12/0.01	1.65/1.09	0.66//0.18	
Y1-3	0.99/0.99	0.93/0.99	0.86/0.98	0.07/0.01	1.72/1.09	0.70//0.18	
Y1-4	0.99/0.99	0.90/0.99	0.82/0.97	0.10/0.01	1.63/1.10	0.68//0.21	
Y1-5	0.99/0.99	0.87/0.99	0.78/0.97	0.13/0.01	1.65/1.09	0.66//0.20	
Y1-6	0.99/0.99	0.91/0.99	0.83/0.97	0.09/0.01	1.71/1.10	0.69//0.19	
Y1-7	0.99/0.99	0.88/0.98	0.79/0.97	0.12/0.02	1.74//1.11	0.67//0.22	
Y1-8	0.99/0.99	0.89/0.98	0.80/0.97	0.11/0.02	1.62/1.10	0.67/0.19	

Table 4. Characteristics of the generalized dimension from adsorption.

spectrum graphs of the 8 samples are in the shape of an upward-opening parabola and all have an asymmetric distribution. Each spectrum can be divided into two branches, the left branch corresponding to the high-probability measurement area, where $f(\alpha)$ increases sharply with the increase of α , and the right branch representing the low-probability measurement area, where $f(\alpha)$ decreases with the increase of α . $\Delta \alpha = \alpha(-10) - \alpha(10)$ reflects the heterogeneity of the sample's pore size distribution, and the larger the value, the stronger the heterogeneity.

Figure 7 shows the relationship between the multifractal dimension D_q and the variable q. As q increases, the value of D_q gradually decreases. According to its trend, the graph can be divided into two segments. In the low-probability measurement area, as q increases, D_q decreases significantly, and in the high-probability measurement area, as q increases, the value of D_q decreases, and the trend tends to be flat.

According to the graph, D0 > D1 > D2 for all samples (Table 4), which reflects that all samples have obvious multifractal characteristics. Among them, D0 is defined as the capacity dimension or box-counting dimension, which reflects the average distribution of the structure; D1 is the information dimension, which is a measure of the concentration of the pore size distribution; D2 (D2 = 2H - 1, H is the HUST index) is the correlation dimension, which represents the scaling behavior at the second sampling moment 16 . $\Delta D = D_{min} - D_{max}$ is the degree of curvature of the generalized size curve, and the larger the value, the stronger the heterogeneity of the pore structure 46 .

Discussion

Pore structure heterogeneity comparison with different methods

Due to the inconsistent detection range, the heterogeneity of pore structure derived from HMIP and LPN_2A methods is different (Table 5). No significant correlation was observed between the multifractal parameters of HMIP and LPN_2A results (Fig. 8). However, the pore structure heterogeneity from HMIP is much stronger than that from LPN_2A . This can be attributed to the significant contribution of smaller pores (pore diameter <10 nm). Compared to the HMIP method, the detection pore diameter range of the LPN_2A method is narrower. Therefore, the combination of the two methods can more accurately characterize the pore structure of the samples, thereby more accurately characterizing the pore structure and structural heterogeneity of shale.

	HMIP/LPN ₂	A				
Sample no.	Н	$\triangle D$	Δα			
Y1-1	0.984/0.924	0.213/0.925	0.316/0.723			
Y1-2	0.988/0.898	0.182/0.982	0.293/0.702			
Y1-3	0.988/0.928	0.180/1.017	0.286/0.817			
Y1-4	0.986/0.910	0.206/0.947	0.326/0.701			
Y1-5	0.987/0.892	0.200/0.993	0.320/0.700			
Y1-6	0.987/0.915	0.192/1.017	0.306/0.783			
Y1-7	0.984/0.897	0.221/1.072	0.335/0.799			
Y1-8	0.986/0.899	0.190/0.959	0.287/0.682			

Table 5. Comparison of pore structure heterogeneity between *HMIP* and *LPN*₂*A* methods.

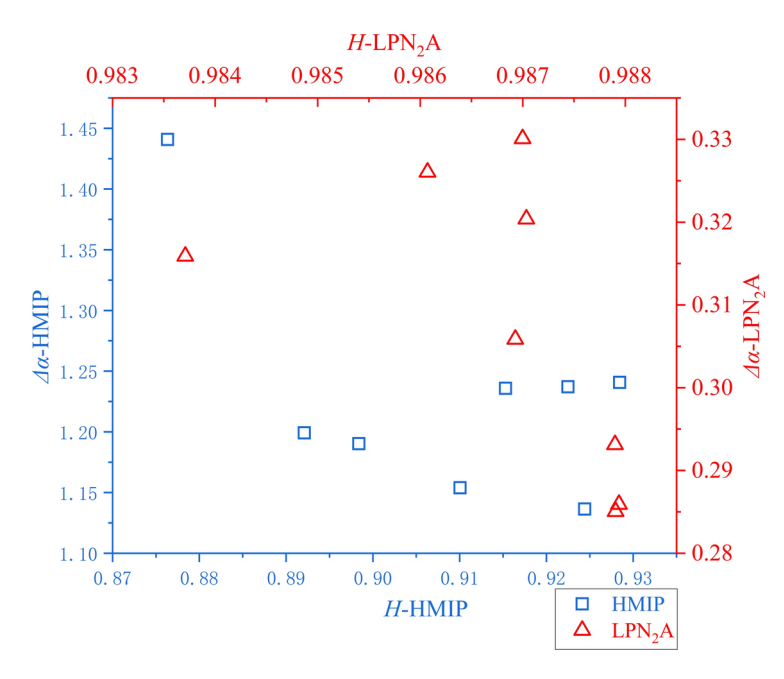


Fig. 8. The relationship between multifractal parameters of LPN₂A and HMIP pore structure.

Relationship of pore structures and multifractal parameters

Figure 9 shows the correlation between H (this parameter describes the statistical self-similarity and long-range dependence of a time series or spatial structure), ΔD (the multifractal dimension ΔD ranges from (– 10, 10) and provides insights into the complexity of the pore structure), $\Delta \alpha$ (the singularity strength $\Delta \alpha$ ($\alpha_{max} - \alpha_{min}$), also known as the multifractal spectrum width, is an important parameter that reflects the degree of heterogeneity in porous media)⁵⁵, and total pore volume and total surface area. For the pore size range measured by the HMIP method, the total pore volume has little effect on the connectivity of pore size distribution, but has a relative strong correlation with the degree of heterogeneity of the pore structure^{15,56}. The H value does not show a clear trend with the increase of total pore volume, indicating that the connectivity of pores is not significantly related to the pore volume, and is mainly influenced by the throat ^{15,56}. The increase in total pore volume leads to an increase in the heterogeneity and complexity of the pore diameter.

The Pearson correlation 57,58 is used to analyze the effect of the size of pore on the multifractal dimension parameters (Fig. 10a).

The relationship between the pores measured by LPN_2A and the multifractal parameters is relatively weak. Among them, the increase in micropore volume enhances the heterogeneity of the pore structure and pore size distribution, and strengthens the connectivity between pores. Meso-pores and macro-pores have the greatest impact on the multifractal characteristics of pore distribution. The increase in meso-pores and macro-pores potentially reduces the connectivity of pores, and the increase in macro-pores enhances the heterogeneity of the pore structure and pore size distribution.

The meso-pores and macro-pores measured by the *HMIP* method have the most significant impact on the pore connectivity and the multifractal parameters of pore distribution (Fig. 10b). The results indicate that the increase in meso-pores leads to poorer pore connectivity and reduced heterogeneity, while the increase in macro-pores enhances pore connectivity and reduces heterogeneity. These results suggest that the increase

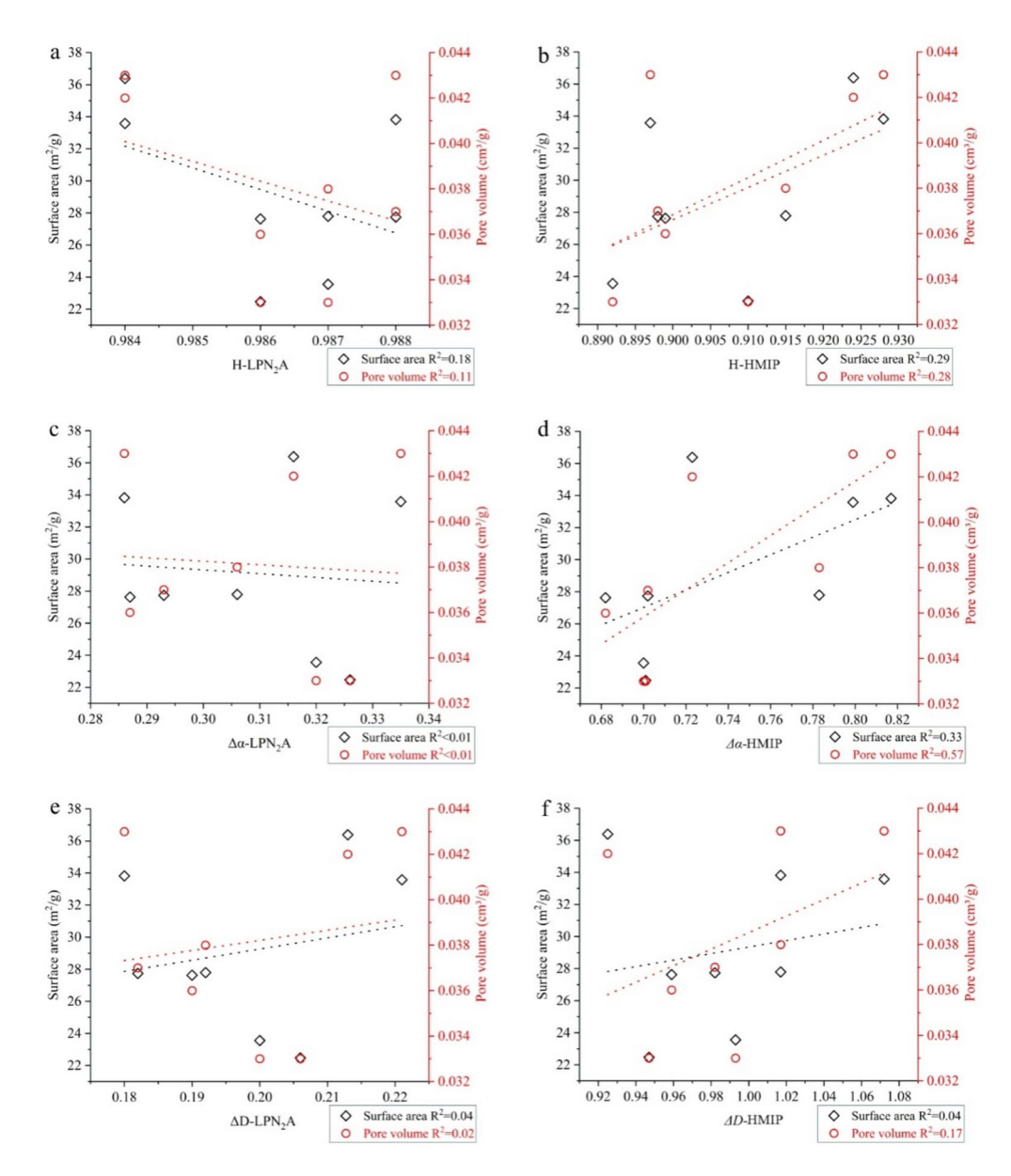


Fig. 9. The relationship between multifractal parameters of LPN_2A and HMIP pore structure.

in macro-pores tends to improve pore connectivity and reduce the complexity of the pore structure, thereby decreasing the heterogeneity of the pore distribution.

Relationship of shale components and multifractal parameters

Figure 11 reflects the relationship between mineral content in shale and multifractal parameters. As the Total Organic Carbon (*TOC*) increases, organic-rich shales typically have a more complex and intense hydrocarbon generation process, which is accompanied by the formation of more complex and numerous micro- and nanopores within the shale. Due to the negative impact of the aforementioned micro-pores on the pore structure and pore size distribution, the pore connectivity decreases and the pore structure becomes more complex with the increase of *TOC*.

The influence of various mineral components in shale on the pore size distribution is shown in the table. The content of quartz in shale has a strong impact on the heterogeneity of the pore size distribution measured by the LPN_2A method, while other minerals have a relatively small impact on the pore heterogeneity. The main reason is the complexity of quartz types in shale, including detrital quartz, microcrystalline quartz, and biogenic quartz. The morphological differences among different types of quartz are significant, and the surface of detrital quartz is prone to dissolution. At the same time, the pore size range measured by the LPN_2A method is limited, thus it has a significant impact on the heterogeneity of the pore size distribution.

The components of shale have a high correlation with the multifractal analysis parameters of the *HMIP* pore characteristics. The higher the content of quartz, the worse the pore connectivity, but its impact on the

Note: MIC~ micro-pores; MES~ meso-pores; MAC~ macro-pores

Fig. 10. Pearson correlation coefficient of multifractal parameters with different pore sizes. (a) LPN_2A ; (b) HMIP.

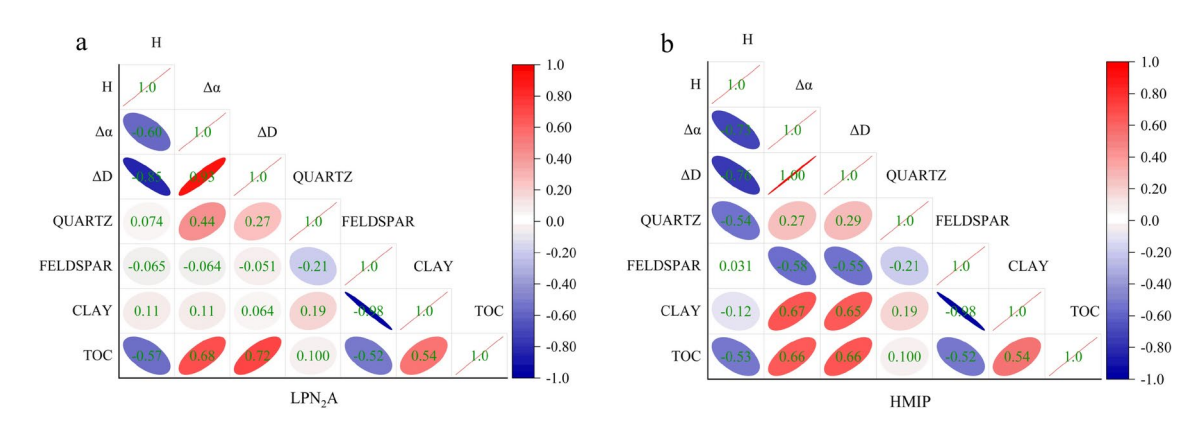


Fig. 11. Pearson correlation coefficient of multifractal parameters with different mineral components. (a) $LPN_{\gamma}A$; (b) HMIP.

heterogeneity of the pores is relatively weak. The main reason is that quartz is mostly filled within the pores, so the presence of quartz reduces the connectivity of the pores. Similar to the LPN_2A method, quartz plays a positively correlated role in the heterogeneity of the pore size distribution and pore morphology. The difference in its impact on the pore size distribution is mainly due to the different pore size distributions measured by the two methods. There is a weak to high correlation between different clay minerals and fractal dimensions, indicating the complexity of the impact of clay minerals on non-micropores. Clay minerals mainly develop non-micropores, but their types have specific pore size distribution characteristics. Clay minerals such as illite, kaolinite, and chlorite each have their own dominant pore size distribution and oriented pore morphology, increasing the complexity of the non-micropore structure of shale. Feldspar in shale is mainly of detrital origin with a small amount of authigenic origin. Detrital feldspar has varying degrees of dissolution and replacement. The formation of feldspar is conducive to the development of meso-pores and macro-pores, therefore, as the content of feldspar increases, the size and morphology of the pores in shale tend to be more homogeneous.

Conclusions

This paper analyzed multifractal characteristics of HMIP and LPN_2A data for eight shale samples from Songliao Basin, focusing on the relationship between multifractal parameters and physical properties. Key findings include:

- (1) The multifractal parameters obtained by the *HMIP* and *LPN*₂*A* methods are different and show no significant correlation. The heterogeneity of the pore structure calculated by the *LPN*₂*A* method is significantly smaller than that obtained by the *HMIP* method.
- (2) Total pore volume and specific surface area have minimal impact on multifractal parameters. LPN₂A: Micropore volume enhances heterogeneity and connectivity; meso- and macro-pores reduce connectivity and increase heterogeneity. HMIP: Meso-pores decrease connectivity and heterogeneity; macro-pores improve connectivity and simplify pore structure.

(3) As TOC increases, shale with high organic matter undergoes more complex kerogen maturation, generating more intricate micro- and nano-pores. This complexity negatively impacts pore connectivity and structure. Quartz content significantly affects pore distribution heterogeneity due to type diversity and surface dissolution, reducing connectivity but having a smaller impact on heterogeneity. Clay minerals and feldspar add complexity to the non-micropore structure; their increase benefits meso- and macro-pore development, leading to more homogeneous pore size and morphology. The correlation coefficient between the multifractal dimension and pore size of *HMIP* is higher than that of *LPN*, A.

Data availability

The data that support the findings of this study are available on request from the corresponding author. The data are not publicly available due to privacy or ethical restrictions.

Received: 4 November 2024; Accepted: 4 March 2025

Published online: 06 March 2025

References

- 1. Liu, D. et al. A new insight into coalbed methane occurrence and accumulation in the Qinshui Basin, China. *Gondwana Res.* 111, 280–297 (2022).
- 2. Ouerghi, F. H., Omri, M., Menaem, A. A., Taloba, A. I. & Abd El-Aziz, R. M. Feasibility evaluation of wind energy as a sustainable energy resource. *Alex. Eng. J.* 106, 227–239. https://doi.org/10.1016/j.aej.2024.06.055 (2024).
- 3. Wang, Y. J., Ma, F., Xie, H. P., Wang, G. L. & Wang, Z. H. Fracture characteristics and heat accumulation of Jixianian carbonate reservoirs in the Rongcheng geothermal field, Xiong'an new area. *Acta Geol. Sin.* 95(6), 1902–1914 (2021).
- Ma, Y. et al. Geological characteristics and exploration practices of continental shale oil in China. Acta Geol. Sin 96(1), 155–171 (2022).
- 5. Administration, U. E. I. Annual energy outlook 2019 with projections to 2050. In *Annual energy outlook 2019 with projections to 2050* 44(8), 1–64 (2019).
- 6. Wang, Y., Liu, D., Cai, Y., Yao, Y. & Pan, Z. Constraining coalbed methane reservoir petrophysical and mechanical properties through a new coal structure index in the Southern Qinshui Basin, Northern China: Implications for hydraulic fracturing. *Aapg Bull.* 104(8), 1817–1842 (2020).
- 7. Jiang, F. et al. Fractal analysis of shale pore structure of continental gas shale reservoir in the Ordos Basin, NW China. *Energy Fuels* **30**(6), 4676–4689 (2016).
- 8. Li, Z. et al. Flow regime transition of multicomponent oil in shale nanopores. Fuel 359, 130431 (2024).
- 9. Chen, H. et al. Experimental simulation of enhanced oil recovery on shale rocks using gas injection from material to characterization: challenges and solutions. *Fuel* **356**, 129588. https://doi.org/10.1016/j.fuel.2023.129588 (2024).
- Feng, Q., Xu, S., Xing, X., Zhang, W. & Wang, S. Advances and challenges in shale oil development: A critical review. Adv. Geo-Energy Res. 4(4), 406–418. https://doi.org/10.46690/ager.2020.04.06 (2020).
- Zhang, Y. et al. Fabrication and verification of a glass-silicon-glass micro-/nanofluidic model for investigating multi-phase flow in shale-like unconventional dual-porosity tight porous media. Lab Chip 19(24), 4071-4082 (2019).
- 12. Wang, Y., Xie, H. & Chen, S. Petrophysical and mechanical properties of complex structure coalbed methane reservoir: A laboratory investigation. *Rock Mech. Rock Eng.* **56**(1), 69–87 (2023).
- 13. Li, H. Research progress on evaluation methods and factors influencing shale brittleness: A review. *Energy Rep.* **8**, 4344–4358 (2022).
- 14. Li, H., He, S., Radwan, A. E., Xie, J. & Qin, Q. Quantitative analysis of pore complexity in lacustrine organic-rich shale and comparison to marine shale: Insights from experimental tests and fractal theory. *Energy Fuels* 38(17), 16171–16188 (2024).
- 15. Zhang, N. et al. Pore structure and fractal characteristics of coal-measure sedimentary rocks using nuclear magnetic resonance (NMR) and mercury intrusion porosimetry (MIP). *Energies* 16(9), 3812. https://doi.org/10.3390/en16093812 (2023).
- 16. Wang, X. et al. Full-scale pore structure and fractal dimension of the Longmaxi shale from the southern Sichuan basin: Investigations using FE-SEM, gas adsorption and mercury intrusion porosimetry. *Minerals* **9**(9), 543 (2019).
- 17. Han, B. B., Qin, Y., Zhang, Z. Study on coal compressibility and correction of compression amount based on compressibility of mercury injection test. *Coal Sci. Technol.* 3 (2015).
- 18. Li, Y. H., Lu, G. Q. & Rudolph, V. Compressibility and fractal dimension of fine coal particles in relation to pore structure characterisation using mercury porosimetry. *Part. Syst. Charact.: Meas. Descr. Part. Prop. Behav. Powders Other Disperse Syst.* 16(1), 25–31 (1999).
- 19. Cai, Y., Li, Q., Liu, D., Zhou, Y. & Lv, D. Insights into matrix compressibility of coals by mercury intrusion porosimetry and N2 adsorption. *Int. J. Coal Geol.* 200, 199–212. https://doi.org/10.1016/j.coal.2018.11.007 (2018).
- 20. Chen, J., Qiu, Y., Qian, Y. & Fang, X. Matrix compressibility and its controlling factors of the marine shale gas reservoir: A case study of the Ning228 Well in the Southwest Sichuan Basin, China. *Processes* 11, 2136 (2023).
- Kuila, U. & Prasad, M. Specific surface area and pore-size distribution in clays and shales. Geophys. Prospect. 61(2), 341–362. https://doi.org/10.1111/1365-2478.12028 (2013).
- 22. Thommes, M. et al. Physisorption of gases, with special reference to the evaluation of surface area and pore size distribution (IUPAC technical report). *Pure Appl. Chem.* 87(9–10), 1051–1069. https://doi.org/10.1515/pac-2014-1117 (2015).
- 23. Hutchinson, J. E. Fractals and self similarity. *Indiana Univ. Math. J.* 30(5), 713–747 (1981).
- 24. Chen, Y. Y., Zou, C. N., Hu, S. Y., Zhu, R. K. & Bai, B. Fractal characteristics of shales across a maturation gradient. *Acta Geol. Sin.* 1, 13–15 (2015).
- 25. Xu, L., Zhang, D. & Xian, X. Fractal dimensions of coals and cokes. J. Colloid Interface Sci. 190(2), 357-359 (1997).
- Garbacz, J. K. Fractal description of partially mobile single gas adsorption on energetically homogeneous solid adsorbent. Colloids Surf. A: Physicochem. Eng. Asp. 143(1), 95–101 (1998).
- 27. Nakagawa, T., Komaki, I., Sakawa, M. & Nishikawa, K. Small angle X-ray scattering study on change of fractal property of Witbank coal with heat treatment. *Fuel* **79**(11), 1341–1346 (2000).
- 28. Gauden, P. A., Terzyk, A. P. & Rychlicki, G. The new correlation between microporosity of strictly microporous activated carbons and fractal dimension on the basis of the Polanyi-Dubinin theory of adsorption. *Carbon* 2, 267–278 (2001).
- 29. Hu, S. et al. Correlation characteristics and simulations of the fractal structure of coal char. Commun. Nonlinear Sci. Numer. Simul. 9(3), 291–303 (2004).
- 30. Song, H. et al. Fractal characteristic of three Chinese coals. Fuel 83(10), 1307–1313 (2004).

| https://doi.org/10.1038/s41598-025-93078-2

- Gould, D. J., Vadakkan, T. J. & Poche, R. A. Multifractal and lacunarity analysis of microvascular morphology and remodeling. Microcirculation 2, 136–151 (2011).
- 32. Ge, X., Fan, Y., Li, J. & Zahid, M. A. Pore structure characterization and classification using multifractal theory—An application in Santanghu Basin of Western China. *J. Pet. Sci. Eng.* 127, 297–304 (2015).

- 33. Liu, K. & Ostadhassan, M. Quantification of the microstructures of Bakken shale reservoirs using multi-fractal and lacunarity analysis. J. Nat. Gas Sci. Eng. 39, 62-71 (2017).
- 34. Chen, X., Yao, G., Cai, J., Huang, Y. & Yuan, X. Fractal and multifractal analysis of different hydraulic flow units based on micro-CT images. J. Nat. Gas Sci. Eng. 48, 145-156. https://doi.org/10.1016/j.jngse.2016.11.048 (2017).
- 35. Li, J. et al. Shale pore characteristics and their impact on the gas-bearing properties of the Longmaxi formation in the Luzhou area. Sci. Rep. 14(1), 16896 (2024).
- 36. Li, W., Liu, H. & Song, X. Multifractal analysis of Hg pore size distributions of tectonically deformed coals. Int. J. Coal Geol. 144, 138-152 (2015).
- 37. Liu, B. et al. Sealing mechanisms in volcanic faulted reservoirs in Xujiaweizi Extension, Northern Songliao Basin, Northeastern China. AAPG Bull. 105(8), 1721-1743 (2021).
- 38. Wei, H.-H., Liu, J.-L. & Meng, Q.-R. Structural and sedimentary evolution of the Southern Songliao Basin, Northeast China, and implications for hydrocarbon prospectivity. AAPG Bull. 94(4), 531-564 (2010).
- 39. Wan, X. et al. Late cretaceous stratigraphy, Songliao Basin, NE China: SK1 cores. Palaeogeogr., Palaeoclimatol., Palaeoecol. 385, 31-43 (2013)
- 40. Feng, Y. et al. Tectonic and climatic influences on architecture of sequences and sedimentary systems in a post-rift basin: Insight from late cretaceous Northern Songliao Basin. Diqiu Kexue - Zhongguo Dizhi Daxue Xuebao/Earth Science-J. China Univ. Geosci. 10, 3445-3461 (2018)
- 41. Song, Y., Ren, J., Stepashko, A. A. & Li, J. Post-rift geodynamics of the Songliao Basin, NE China: Origin and significance of T11 (Coniacian) unconformity. Tectonophysics 634, 1-18 (2014).
- 42. Zhu, J. et al. Decoding stratigraphic and structural evolution of the Songliao Basin: Implications for late Mesozoic tectonics in NE China. J. Asian Earth Sci. 194, 104138 (2020).
- 43. Li, S. Q. et al. Late Mesozoic tectonic evolution of the Songliao Basin, NE China: Evidence from detrital zircon ages and Sr-Nd isotopes. Gondwana Res. 22(3-4), 943-955 (2012).
- 44. Zhang, F. Q., Dilek, Y., Chen, H. L., Yang, S. F. & Meng, Q. A. Structural architecture and stratigraphic record of late Mesozoic sedimentary basins in NE China: Tectonic archives of the Late Cretaceous continental margin evolution in east Asia. Earth-Sci. Rev. 171, 598-620 (2017).
- 45. Feng, Z. Q. et al. Tectonostratigraphic units and stratigraphic sequences of the Nonmarine Songliao Basin, Northeast China. Basin Res. 22(1), 79-95. https://doi.org/10.1111/j.1365-2117.2009.00445.x (2010).
- 46. Liu, B. et al. Lithofacies and depositional setting of a highly prospective lacustrine shale oil succession from the upper cretaceous Qingshankou formation in the Gulong Sag, Northern Songliao Basin, Northeast China. Aapg Bull. 103(2), 405–432 (2019).
- 47. Li, M. et al. Compositional differences of near-critical petroleum from closed pores to wellhead in Gulong shale oil play, Songliao Basin, NE China. Mar. Pet. Geol. 167, 106968. https://doi.org/10.1016/j.marpetgeo.2024.106968 (2024).
- Sun, Y. et al. Multifractal analysis and neural network prediction of pore structures in coal reservoirs based on NMR T, spectra. Energy Fuels 35(14), 11306-11318 (2021).
- 49. Zhao, Y. et al. Multifractal analysis of coal pore structure based on NMR experiment: A new method for predicting T₂ cutoff value. Fuel 283, 119338 (2021).
- 50. Halsey, T. C., Jensen, M. H., Kadanoff, L. P., Procaccia, I. & Shraiman, B. I. Fractal measures and their singularities: The characterization of strange sets. Phys. Rev. A, Third Ser. 2, 1141-1151 (1986)
- 51. Chhabra, A. & Jensen, R. V. Direct determination of the f(α) singularity spectrum. Phys. Rev. Lett. 62(12), 1327–1330. https://doi. org/10.1103/PhysRevLett.62.1327 (1989).
- 52. Hou, X., Zhu, Y., Chen, S., Wang, Y. & Liu, Y. Investigation on pore structure and multifractal of tight sandstone reservoirs in coal bearing strata using LF-NMR measurements. J. Pet. Sci. Eng. 187, 106757 (2020).
- 53. Zheng, S. et al. Nuclear magnetic resonance T2 cutoffs of coals: A novel method by multifractal analysis theory. Fuel 241, 715-724
- 54. Song, Z. et al. Multi-fractal distribution analysis for pore structure characterization of tight sandstone—A case study of the upper Paleozoic tight formations in the Longdong district, Ordos Basin. Mar. Pet. Geol. 92, 842-854 (2018)
- 55. Salat, H., Murcio, R. & Arcaute, E. Multifractal methodology. Phys. A: Stat. Mech. Appl. 473, 467-487. https://doi.org/10.1016/j.ph
- 56. Liu, K. et al. Multifractal analysis of gas adsorption isotherms for pore structure characterization of the Bakken Shale. Fuel 219, 296-311. https://doi.org/10.1016/j.fuel.2018.01.126 (2018).
- 57. Daniels, H. E. The relation between measures of correlation in the universe of sample permutations. Biometrika One Hundred Years 33, 247-254 (2001).
- 58. Pearson, K. V. I. I. Note on regression and inheritance in the case of two parents. Proc. R. Soc. London 58(347-352), 240-242 (1895).

Acknowledgements

This research was supported by the Fundamental Research Funds for the Central Universities (https://doi.org/10 .13039/501100012226) * JZ2023HGTA0177 * JZ2023HGQA0146 National Natural Science Foundation of China (https://doi.org/10.13039/501100001809) * 42002189.

Author contributions

C.S. wrote the main manuscript text, L.D. and W.J. wrote and reviewed the manuscript, Z.W., Z.Q. and Y.X. prepared figures and tables. All authors agreed with submission to the Scientific Report for publication.

Declarations

Competing interests

The authors declare no competing interests.

Ethical approval

This article does not contain any studies with animals performed by any of the authors.

Additional information

Correspondence and requests for materials should be addressed to D.L.

Reprints and permissions information is available at www.nature.com/reprints.

(2025) 15:7866

Scientific Reports |

Publisher's note Springer Nature remains neutral with regard to jurisdictional claims in published maps and institutional affiliations.

Open Access This article is licensed under a Creative Commons Attribution-NonCommercial-NoDerivatives 4.0 International License, which permits any non-commercial use, sharing, distribution and reproduction in any medium or format, as long as you give appropriate credit to the original author(s) and the source, provide a link to the Creative Commons licence, and indicate if you modified the licensed material. You do not have permission under this licence to share adapted material derived from this article or parts of it. The images or other third party material in this article are included in the article's Creative Commons licence, unless indicated otherwise in a credit line to the material. If material is not included in the article's Creative Commons licence and your intended use is not permitted by statutory regulation or exceeds the permitted use, you will need to obtain permission directly from the copyright holder. To view a copy of this licence, visit https://creativecommons.org/licenses/by-nc-nd/4.0/.

© The Author(s) 2025